

# An Adaptive Multirate Algorithm for Acquisition of Fluorescence Microscopy Data Sets

Thomas E. Merryman, *Student Member, IEEE*, and Jelena Kovačević, *Fellow, IEEE*

**Abstract**—We propose an algorithm for adaptive efficient acquisition of fluorescence microscopy data sets using a multirate (MR) approach. We simulate acquisition as part of a larger system for protein classification based on their subcellular location patterns and, thus, strive to maintain the achieved level of classification accuracy as much as possible. This problem is similar to image compression but unique due to additional restrictions, namely causality; we have access only to the information scanned up to that point. While we do want to acquire fewer samples with as low distortion as possible to achieve compression, our goal is to do so while affecting the overall classification accuracy as little as possible. We achieve this by using an adaptive MR scanning scheme which samples the regions of the image area that hold the most pertinent information. Our results show that we can achieve significant compression which we can then use to acquire faster or to increase space resolution of our data set, all while minimally affecting the classification accuracy of the entire system.

## I. INTRODUCTION

THE motivation for finding an efficient way of acquiring cellular data sets is great. In fluorescence microscopy, the confocal laser scanning microscope is one of the most often used and it scans the field line-by-line, pixel-by-pixel [1], [2]. Photobleaching occurs each time the laser used to excite the region being imaged focuses on a pixel. The exposure time and laser intensity both play a major part in photobleaching. By reducing the number of samples we need to scan, we avoid the unnecessary exposure of the specimen to light, as well as save time and, thus, speed up the acquisition process [3]. One could reduce the number of samples acquired by using traditional sampling algorithms but effects of aliasing would distort the approximation data sets [4]. We aim here for an adaptive, efficient algorithm that would scan fewer pixel locations, while limiting the distortion and maintaining as much information as possible about the distribution of fluorescence in the sample. This requires some means of evaluation, and for this we build on prior work demonstrating that machine classifiers can recognize all major subcellular patterns in three-dimensional (3-D) data sets of cultured cells with high accuracy as shown by Murphy and his group [5]–[8]. We can, thus, compare the classification accuracy for

adaptively sampled data sets to that for the original data sets to assess the degree of preservation of image information content.

The bulk of previous work in this area focused on the process of recovery rather than data acquisition [11]–[13]. There exist some examples of undersampling of cellular fields by simple approaches such as scanning every other line or every fourth line in a line-by-line scanning pattern [9]. This approach could be described as efficient but most certainly not adaptive as it does not change with the input of the field. Trying to efficiently acquire cellular data sets using adaptive sampling methods is new.

We will work both with two-dimensional (2-D) data sets (slices of cell volumes) and 3-D data sets (cell volumes) of maximum resolution [6] in each of the three dimensions and will run our multirate (MR) data acquisition algorithm using different input parameters on each of these data sets to simulate the real acquisition process. MR in this paper refers to processing at different sampling rates specific to the content present in those regions. We will then compare our adaptively sampled data sets to the original data sets and examine their rate-distortion curves to find where the algorithm works optimally. We will do the same with standard downsampling (regular sampling in each dimension) using bilinear interpolation. Although this rate-distortion measure will give a general insight into the performance of the algorithm, our goal is to eventually reduce the number of samples while minimally affecting the classification accuracy of the system. We will, thus, measure the compression ratio with respect to the classification accuracy. Eventually, our algorithm should serve as a model for guiding the microscope's scanning protocol.

## II. MOLECULAR IMAGING

For each pixel in the cellular field, a length of time is required to excite the fluorophores present in order to emit light. The exposure time is dependent on the intensity of the laser. As illustrated in Fig. 1, the laser passes through an objective and is concentrated in the focal plane. Although the energy of the laser converges in the focal plane, the laser must still pass through the planes neighboring the focus plane. This exposure to the laser causes photobleaching effects in the neighboring planes. By acquiring fewer samples, we could reduce the intensity of the laser, thereby reducing the effects of photobleaching. The reduced number of samples could also be used to speed up the acquisition of cellular data sets when implemented on a confocal scanning microscope.

Fig. 2 gives a representative image from our data sets. Observe how the image is predominantly dark with mostly low pixel intensities. We, thus, assume the following: High

Manuscript received December 12, 2004; revised May 20, 2005. This work was supported in part by the NSF ITR under Grant EF-0331657. Parts of this material were presented at ICASSP'05, Philadelphia, PA. The associate editor coordinating the review of this manuscript and approving it for publication was Dr. Gaudenz Danuser.

T. E. Merryman is with the Department of Electrical and Computer Engineering, Carnegie Mellon University, Pittsburgh, PA 15213 USA (e-mail: tadm@cmu.edu).

J. Kovačević is with the Department of Biomedical Engineering and the Department of Electrical and Computer Engineering, Carnegie Mellon University, Pittsburgh, PA 15213 (e-mail: jelenak@cmu.edu).

Digital Object Identifier 10.1109/TIP.2005.855861

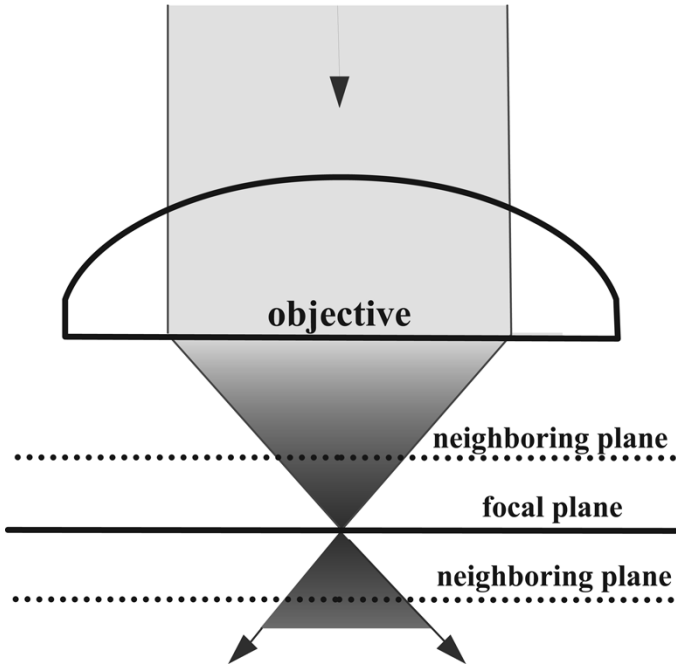


Fig. 1. Laser concentrated on the focal plane. Laser intensity increases near the focal plane.

frequencies (rapid changes in pixel intensities among neighboring pixels) will only occur in a small percentage of the area contained within the image boundaries. Observe also how the neighboring slices share similar shape patterns and locations in the 3-D image of actin given in Fig. 3.

With these observations in mind, we can make a strong argument for a MR approach. When standard downsampling is used and the data set is then interpolated back to the maximum resolution using bilinear interpolation, all of the high-frequency content is lost. In the dark regions of the data sets, only low frequencies are present, which can be captured with only a few samples. In contrast, in the areas where high-intensity values are located, high frequencies reside that need to be represented using a greater number of samples. Thus, using different sampling rates in different areas of the image is warranted. We call this MR sampling.

### III. ALGORITHM FOR MR ACQUISITION OF CELLULAR DATA SETS

An intuitive way to describe the algorithm is to consider the board game Battleship. The player's goal is to locate the exact locations of his/her opponent's ships in the most efficient manner possible. We draw a parallel between the game board grid and the unknown cellular field. Each consists of discrete locations and the pertinent information location is not known upon beginning the search. It would be foolish to play the game in a nonadaptive approach, that is, knowing all of the locations where you will probe *a priori*. For example, if a ship has been hit, one would not continue with predetermined probe locations; rather, one would keep on probing in the area around the hit. Similarly, when acquiring our data sets, we keep on probing around those locations deemed significant. Thus, an

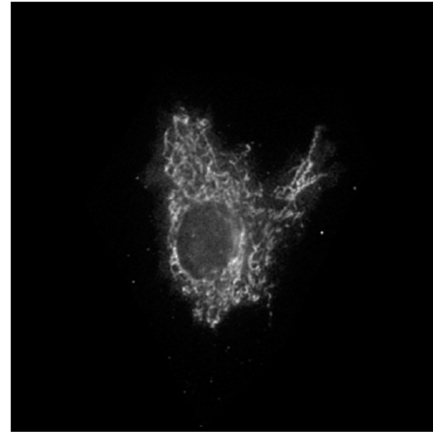


Fig. 2. Image of a mitochondrial protein pattern.

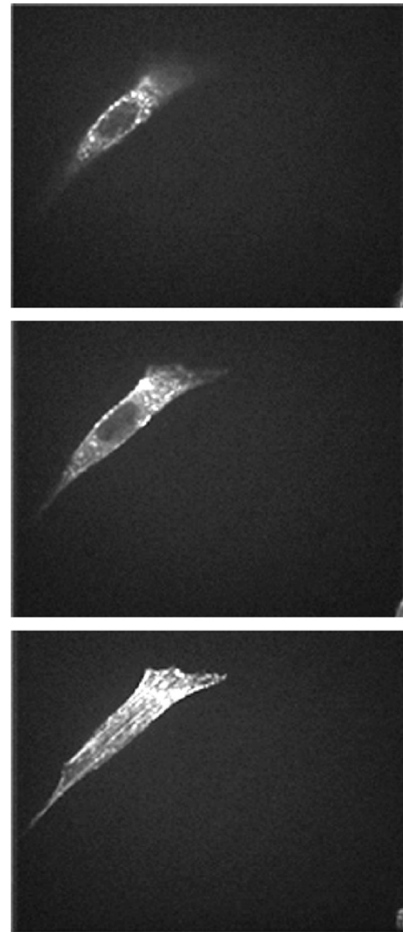


Fig. 3. Images from a 3-D sequence of actin protein pattern.

adaptive MR sampling approach mimics the strategy used in the game.

We denote our 3-D data set as  $x \in \mathbb{R}^{M \times N \times O}$  where  $M = 2^l M_1$ ,  $N = 2^l N_1$  and  $O$  denote the image size in the three spatial dimensions. The block diagram of our adaptive MR algorithm is shown in Fig. 4, and repeated for each slice of the 3-D image. This is the major component of the overall system that constructs an approximation to the original cellular data set. We now explain the algorithm in more detail.

In our simulations, a probe is represented by taking a sample from the maximum resolution original image at a specific pixel location. Probe locations are initialized in one of two ways: The first is to set up probe locations throughout the entire cellular field rectangularly at  $2^l$  primary units apart (primary unit refers to the basic element of the maximum resolution), as in Fig. 5. For our experiments, we set  $l = 3$  or 4. These probe locations belong to the following index set  $I$ :

$$I = \left\{ (m, n) \left| \begin{array}{l} m = 2^{l-1}(2k_m + 1), \quad k_m = 0, \dots, M_1 - 1 \\ n = 2^{l-1}(2k_n + 1), \quad k_n = 0, \dots, N_1 - 1. \end{array} \right. \right.$$

This index set corresponds to the probing image,  $p \in \mathbb{R}^{M \times N}$ . Method (a) is described as

$$p_{m,n,o}^{(a)} = \begin{cases} 1, & (m, n) \in I \\ 0, & \text{otherwise.} \end{cases}$$

Thus,  $p_{m,n,o}^{(a)}$  would be equal to 1 in black box locations in Fig. 5, and 0 everywhere else. The method described above is identical to how the probing locations are set up using standard downsampling.

The second way in which the probe locations are initialized uses cellular location knowledge that has already been acquired from previous slices in the 3-D sequence. For example, Fig. 3, shows that cell locations in adjacent slices are very similar. When stepping through the sampling process, it is efficient to rule out areas unlikely to contain any pertinent information. Fig. 6 shows an illustration of how to initialize the probe locations if we know approximately where the cell is located. We will elaborate on this in what follows. The initialization of these probe locations is identical to the method (a) with one added step—the application of a mask from the previous slice as shown here (the computation of the mask is given later in this section). Thus, the probing image for method (b),  $p_{m,n,o}^{(b)}$  is given by

$$p_{m,n,o}^{(b)} = p_{m,n,o}^{(a)} \cdot \text{mask}_{m,n,o-1}.$$

We can, thus, express the probing image as

$$p_{m,n,o} = \begin{cases} p_{m,n,o}^{(a)}, & \text{method(a)} \\ p_{m,n,o}^{(b)}, & \text{method(b)}. \end{cases}$$

These two methods for initializing the probe locations are used in two different situations: The first method is used when there is no information available about the location of the cell, while the second one is used when such information is available (for example, when slices at either previous time instants or previous locations along the third spatial dimension have already been acquired). To add more robustness to the system, the first method can also be used periodically even when knowledge about the location is available. Probing occurs until there are no more locations left to be examined.

After a location is probed and an intensity value is returned, it is compared to a threshold  $T$ . The threshold is set by the user and determines the sensitivity of the algorithm. A lower threshold will raise the sensitivity and take more samples while a higher threshold will consider more locations to be uninter-

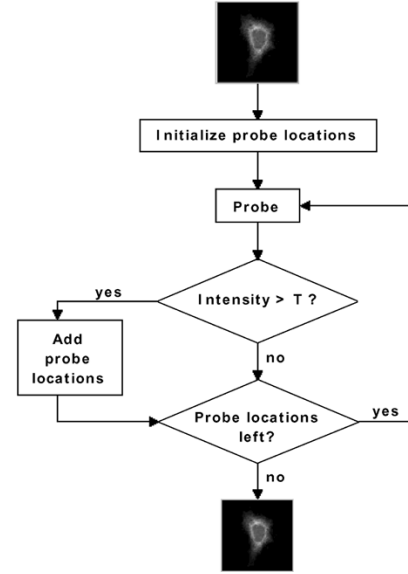


Fig. 4. Block diagram for the MR sampling algorithm.

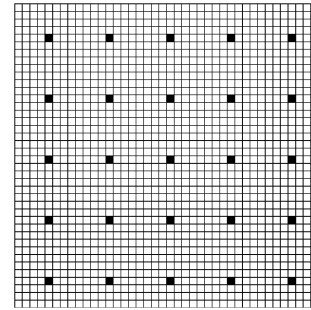


Fig. 5. Initial sampling grid for both the method (a), and the standard downsampling algorithm. Each block represents a possible probe location while the black blocks represent where a probe location has been initialized.

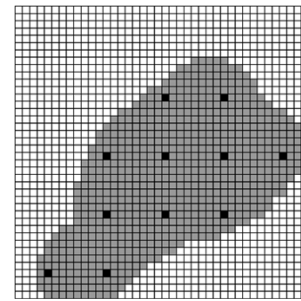


Fig. 6. Initial sampling grid for method (b). Each block represents a possible probe location. Black blocks represent where a probe location has been initialized. Gray blocks represent the locations where we assume important information is located. The probe locations are only set up in the area where the cell is believed to be located.

esting. When a pixel's intensity is examined, one of two things occurs: If the value is greater than the threshold, then the value is stored in what is called a *foreground image*,  $f$ . The foreground image contains all of the intensity values gathered from probes where the intensity exceeds the threshold

$$f_{m,n,o} = \begin{cases} x_{m,n,o}, & x_{m,n,o} > T \& (m, n) \in I \\ 0, & \text{otherwise.} \end{cases}$$

With this image, we associate the binary image  $fb$  where 1 signifies where the foreground image has positive intensities and 0 signifies no intensity

$$fb_{m,n,o} \begin{cases} 1, & f_{m,n,o} > 0 \\ 0, & \text{otherwise.} \end{cases}$$

After the current value exceeding the threshold is stored, new probes are added as shown in Fig. 7. The examined pixel can be thought to have a depth,  $d$ . The extended neighborhood is  $c2^{l-d}$  from the current location. For our experiments,  $c = 1.5$ . In the figure, the distance between probe locations (black pixels) is  $2^l = 8, d = 0$ . In part (a), the gray pixels ( $l = 3, d = 1$ ) represent the probe locations added when the circled probe location reveals a value that is greater than or equal to the threshold. This is a recursive process and its next step is shown in part (b) of the same figure. This operation can also be thought of as the following convolution:

$$p_{m,n,o}^{(\text{new})} = fb * t$$

where  $t_{m,n} \in \mathbb{R}^{(c2^{l-d}+1) \times (c2^{l-d}+1)}$  and

$$t_{m,n} = \begin{cases} 1, & m = 2^{l-d-1}k_m, \quad k_m = 0, \dots, 2c \\ & n = 2^{l-d-1}k_n, \quad k_n = 0, \dots, 2c \\ 0, & \text{otherwise.} \end{cases}$$

For example, with  $l = 3$  and  $c = 1.5$ , we have  $t_{m,n} \in \mathbb{R}^{13 \times 13}$  and it equals 1 only for  $m, n = 0, 4, 8, 12$ .

This process iterates until all of the probe locations identified by  $p$  are probed. The index set  $I$  is also updated at this time

$$I^{(\text{new})} = \left\{ (m, n) \mid p_{m,n,o}^{(\text{new})} = 1 \right\}.$$

We then set  $p = p^{(\text{new})}$  and  $I = I^{(\text{new})}$  in preparation for a new iteration.

Each time a value is returned from a probe it is stored in what is called the background image  $b$ . This occurs regardless of whether or not the value exceeded the threshold. The background image consists of all the probed locations which have then been interpolated to the dimensions of the original image. When a location is probed, the value is placed in a temporary image  $z$  of the same dimensions as the original and initialized to all zeros. The probed value is then replicated to fill its proximity. The proximity is a subset of  $z$  that surrounds the probe location in the neighborhood of  $2^{l-d}$  where  $d$  is once again the depth of the particular index value in  $I$ . All the locations in this subset take on the value of the probed location

$$z_{m+k_m, n+k_n, o} = \begin{cases} x_{m,n,o}, & k_m = -2^{l-d-1}, \dots, 2^{l-d-1} - 1 \\ & k_n = -2^{l-d-1}, \dots, 2^{l-d-1} - 1 \\ & (m, n) \in I. \end{cases}$$

Once all probing is completed, we can now construct the background image  $b$ , given by

$$b_{m,n,o} = (z * lp)_{m,n,o}$$

where  $lp$  is a lowpass filter. In our experiments, we used a simple averaging filter  $lp \in \mathbb{R}^{8 \times 8}$  where  $lp = 1/64$  everywhere.

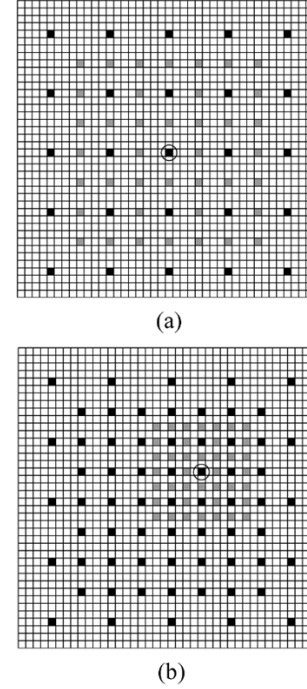


Fig. 7. (a) Grid obtained when the circled probe location returns a value greater than the threshold. When this happens, the probe locations in gray are added. (b) When one of the gray locations from (a) returns an intensity greater than the threshold, the process continues recursively.

Now, we can construct the approximated image equal to the background image where the foreground image is without an intensity value

$$y_{m,n,o} = \begin{cases} f_{m,n,o}, & f_{m,n,o} > 0 \\ b_{m,n,o}, & \text{otherwise.} \end{cases}$$

To create a more efficient algorithm and save even more probes, we can use the information about the cell location from the previous slice that has been approximated. This is done by creating a mask. The mask examines the foreground image of the neighboring/previous slice.

This image is expanded by the morphological operation of dilation to create a mask that is larger than the area where the structure was located in the neighboring slice

$$\text{mask}_{m,n,o} = \begin{cases} 1, & (fb * s)_{m,n,o} > 0 \\ 0, & \text{otherwise} \end{cases}$$

where  $s_{m,n,o} \in \mathbb{R}^{2^l \times 2^l}$ ,  $s_{m,n,o} = 1$  everywhere. This compensates for any growth, movement or displacement of the cell. In the subsequent slice, we will only initialize the probe locations that lie in the region where the mask is located. If we consider our board game example again, it becomes clear how the masking operation works. Let us modify the game so that multiple rounds of the game are allowed. In the subsequent rounds, the opponent's pieces are limited to how far they can travel from the prior round. With this restriction, an efficient search would begin in only those neighborhoods where the opponent's pieces were located in the earlier round. For 2-D cellular data sets, the masking step is omitted. With those data sets, the algorithm never assumes to have knowledge of the cell location and always

initializes the probe locations using the first method of initialization described earlier in this section.

#### IV. DISCUSSION

##### A. Acquisition Time

A 2-D data field having dimensionality  $m \times n$  has  $mn$  total probe locations. Our MR approach reduces the number of probed locations to  $mn/2^{2l} + s$ , where  $s$  is an approximate number of probe locations that exceed the threshold  $T$ . Since  $mn/2^{2l} + s \leq mn$ , the amount of compression depends on  $s$  (determined by  $T$ ), and the data set being acquired.

Typically,  $s \gg mn/2^{2l}$  indicating that the majority of probes in the MR algorithm are spent acquiring data that exceeds the threshold, in which case, the number of probe locations depends more on the number of samples exceeding the threshold and less on the dimensions of the acquisition field. The number of probes for MR will be between  $mn$  (when all samples exceed threshold) and  $mn/2^{2l-1}$  (when  $s$  approaches  $mn/2^{2l}$ ). Each pixel probed in a data set requires an excitation time for the fluorescence to be detected by the microscope. The excitation time cost is proportional to the percentage of samples kept, that is, to  $1/2^{2l} + s/(mn)$ .

Excitation time will be faster for the data set proportional to the number of samples kept, a factor of  $1/2^{2l} + s/(mn)$ . The time associated with adding additional probes is of  $O(1)$ , a negligible amount. The increased acquisition time cost depends solely on the confocal scanning microscope's ability to change laser spot.

##### B. Data Storage

The data storage requirement of this system is similar to that of the normal, line-by-line, pixel-by-pixel acquisition. The output of the MR system is a data set that matches the dimensions of the total cellular field being captured. This approximated data set has the same dimensionality as the original data set. Since the MR algorithm approximates the original data set, there is no further saving in terms of storage.

##### C. Distortion of Input

The distortion of input is an important topic and is discussed in greater detail in Section V. We compare our simulated acquisition to the simulations of nonadaptive approaches and observe the distortion in both a mean-squared error (MSE) and classification sense.

##### D. Robustness to Noisy Input

The MR acquisition is not impervious to noise. If the cellular field being imaged is noisy, then the MR algorithm will use additional samples to capture noisy areas. The amount of noise captured will depend on the noise distribution, intensity of noise and the threshold of acquisition. Thus, the algorithm will adapt itself to a noisy input, probing more samples and resulting in lower overall compression.

##### E. Implementation

Confocal scanning microscopes have the precision to capture any pixel in the cellular field. The cost of implementing this

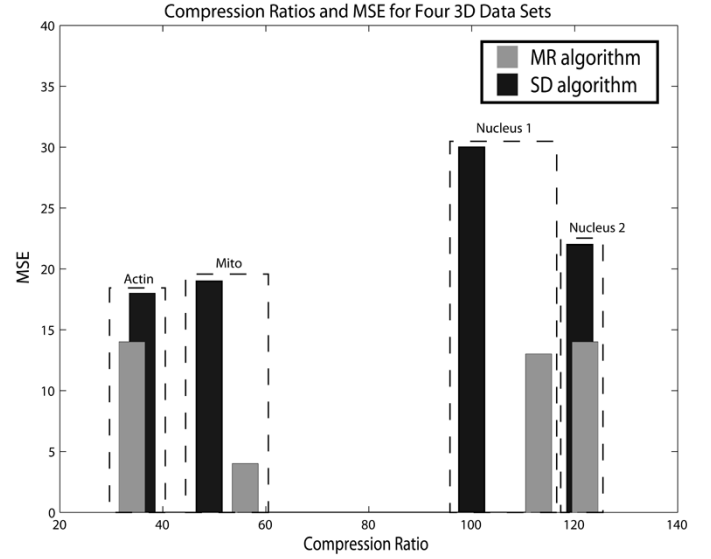


Fig. 8. Compression ratios and MSE for four 3-D data sets. The results are given for the MR algorithm and the standard algorithm.

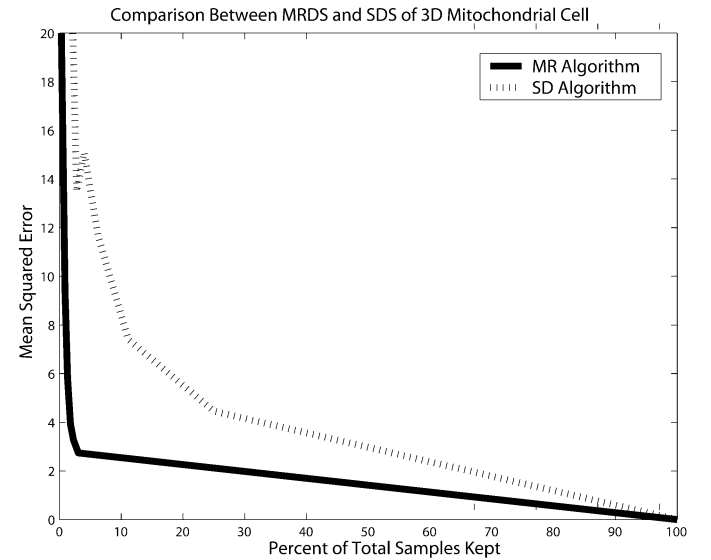


Fig. 9. Rate-distortion curves for MR downsampling compared to standard downsampling with bilinear interpolation.

system is the reprogramming of the microscope to follow a different protocol as explained in Section III, as well as the time needed to move from pixel to pixel. These issues will be addressed in detail during the implementation stage of this project.

#### V. EXPERIMENTAL RESULTS

##### A. Effect of Sampling on MSE

We synthesized the cellular field by using four data sets. Each of the sequences is of size  $1024 \times 1280 \times 30$ . After processing each of the sequences we compared them to the original sequences. We found the MSE for different thresholds which affect the number of samples taken. We also repeated the process with standard downsampling and bilinear interpolation and compared the results. Fig. 8 gives the optimal compression ratio and MSE for the four 3-D data sets we tested. Due to the

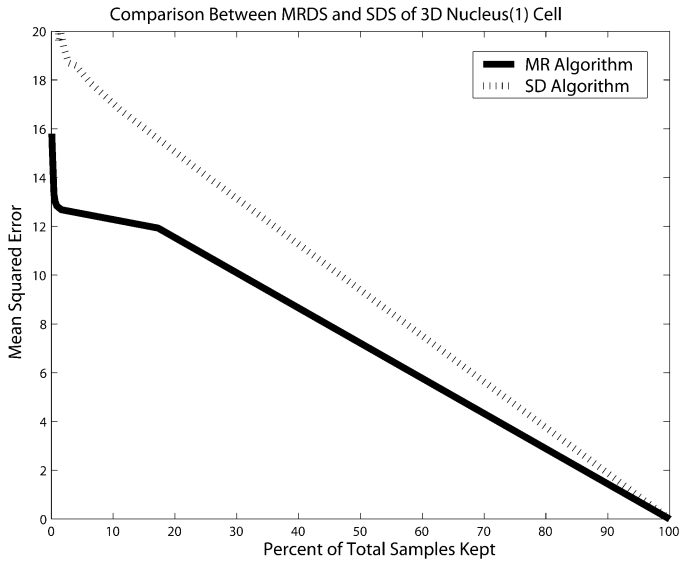


Fig. 10. Rate-distortion curves for MR downsampling compared to standard downsampling with bilinear interpolation.

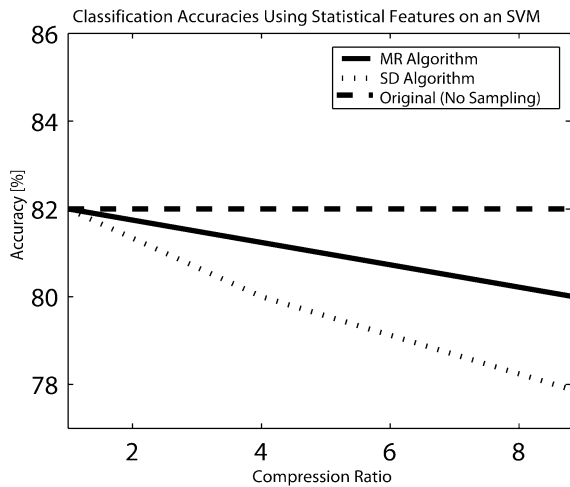


Fig. 11. Classification accuracy of the original system (no sampling), MR algorithm, and standard algorithm, using statistical features and SVM classifier [14].

nature of the two algorithms, we cannot obtain exactly the same compression ratios. Therefore, we find the closest compression ratios we can for the MR algorithm and the standard one and then compare the distortions. This comparison yields a consistently higher distortion for the standard algorithm. The MSE is given by

$$MSE = \frac{1}{MNO} \sum_{m=0}^M \sum_{n=0}^N \sum_{o=0}^O (x_{m,n,o} - y_{m,n,o})^2$$

where  $x$  is the original sequence and  $y$  is the approximated sequence whose values range from 0 to 255. Figs. 9 and 10 show the rate-distortion curves of two of the 3-D image sets from Fig. 8. MR downsampling clearly outperforms standard downsampling with bilinear interpolation.

TABLE I  
DETAILED CLASSIFICATION ACCURACY FOR (a) NO SAMPLING, (b) MR SAMPLING ALGORITHM, AND (c) SD ALGORITHM, USING STATISTICAL FEATURES AND SVM CLASSIFIER [14]

Original Image Accuracy (No Sampling)

| Input | Output of Classifier |    |     |     |    |     |     |     |     |     |
|-------|----------------------|----|-----|-----|----|-----|-----|-----|-----|-----|
|       | DNA                  | ER | Gia | Gpp | L2 | Mit | Nuc | Act | TFR | Tub |
| DNA   | 94                   | 2  | 0   | 0   | 0  | 0   | 0   | 0   | 4   | 0   |
| ER    | 2                    | 82 | 0   | 0   | 2  | 2   | 0   | 0   | 0   | 12  |
| Gia   | 0                    | 0  | 84  | 10  | 0  | 0   | 4   | 0   | 2   | 0   |
| Gpp   | 0                    | 0  | 8   | 80  | 6  | 0   | 2   | 0   | 2   | 2   |
| L2    | 0                    | 0  | 0   | 2   | 80 | 0   | 0   | 0   | 16  | 2   |
| Nuc   | 0                    | 2  | 0   | 0   | 0  | 82  | 0   | 0   | 6   | 10  |
| Mit   | 2                    | 0  | 0   | 0   | 4  | 0   | 92  | 0   | 2   | 0   |
| Act   | 0                    | 0  | 0   | 0   | 0  | 0   | 0   | 100 | 0   | 0   |
| Tfr   | 2                    | 2  | 0   | 0   | 18 | 8   | 0   | 2   | 56  | 12  |
| Tub   | 0                    | 8  | 0   | 0   | 2  | 8   | 0   | 0   | 12  | 70  |

Average Accuracy 82%

Accuracy with MR Algorithm

| Input | Output of Classifier |    |     |     |    |     |     |     |     |     |
|-------|----------------------|----|-----|-----|----|-----|-----|-----|-----|-----|
|       | DNA                  | ER | Gia | Gpp | L2 | Mit | Nuc | Act | TFR | Tub |
| DNA   | 82                   | 2  | 0   | 0   | 2  | 0   | 2   | 0   | 12  | 0   |
| ER    | 4                    | 76 | 0   | 0   | 6  | 0   | 0   | 0   | 2   | 12  |
| Gia   | 0                    | 0  | 84  | 4   | 6  | 0   | 4   | 0   | 2   | 0   |
| Gpp   | 0                    | 0  | 8   | 76  | 10 | 0   | 2   | 0   | 2   | 2   |
| L2    | 0                    | 2  | 0   | 2   | 86 | 0   | 0   | 0   | 10  | 2   |
| Nuc   | 0                    | 4  | 0   | 0   | 2  | 78  | 0   | 0   | 6   | 10  |
| Mit   | 4                    | 0  | 2   | 0   | 4  | 0   | 88  | 0   | 2   | 0   |
| Act   | 0                    | 0  | 0   | 0   | 0  | 0   | 0   | 100 | 0   | 0   |
| Tfr   | 2                    | 2  | 0   | 2   | 18 | 4   | 0   | 2   | 54  | 16  |
| Tub   | 0                    | 8  | 0   | 2   | 4  | 4   | 0   | 0   | 6   | 76  |

Average Accuracy: 80%, Compression Ratio: 9.8:1

Accuracy with SD Algorithm

| Input | Output of Classifier |    |     |     |    |     |     |     |     |     |
|-------|----------------------|----|-----|-----|----|-----|-----|-----|-----|-----|
|       | DNA                  | ER | Gia | Gpp | L2 | Mit | Nuc | Act | TFR | Tub |
| DNA   | 92                   | 2  | 0   | 0   | 0  | 0   | 0   | 0   | 4   | 2   |
| ER    | 2                    | 88 | 0   | 0   | 0  | 0   | 0   | 0   | 0   | 10  |
| Gia   | 0                    | 0  | 82  | 12  | 0  | 0   | 4   | 0   | 2   | 0   |
| Gpp   | 0                    | 0  | 8   | 82  | 6  | 0   | 0   | 0   | 2   | 2   |
| L2    | 0                    | 4  | 0   | 2   | 78 | 0   | 0   | 0   | 16  | 0   |
| Nuc   | 0                    | 6  | 0   | 0   | 2  | 74  | 0   | 0   | 10  | 8   |
| Mit   | 4                    | 0  | 2   | 0   | 2  | 0   | 90  | 0   | 2   | 0   |
| Act   | 0                    | 0  | 0   | 0   | 0  | 0   | 0   | 98  | 2   | 0   |
| Tfr   | 2                    | 2  | 0   | 0   | 16 | 8   | 0   | 6   | 52  | 14  |
| Tub   | 0                    | 8  | 0   | 0   | 2  | 12  | 0   | 0   | 14  | 64  |

Average Accuracy: 80%, Compression Ratio: 4:1

### B. Effect of Sampling on Classification Accuracy

What we look into now is how the classification accuracy is affected by these two algorithms with two separate classifiers. We do these experiments on 2-D data sets only. We use a bank of 500 2-D data sets of size  $512 \times 512$  [7], which represent ten distinct classes of proteins. The first classifier uses statistical features classified by a support vector machine (SVM) [14]. The second classifier uses the 13 texture features proposed by Haralick [15] classified using neural networks.

1) *Statistical Features and SVM Classifier:* We now begin the statistical classification mentioned above by calculating the statistical features for each of the approximated data sets. A

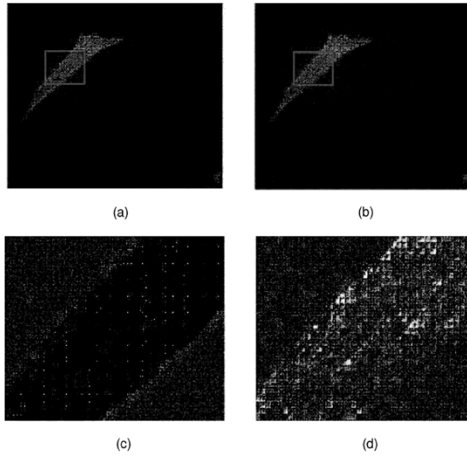


Fig. 12. Illustration of the errors created with each of the sampling schemes. (a) MR approximated image. (b) Standard downsampling approximated image. (c) Differences between the original data sets and the MR sampled image within blue square from (a). (d) Difference between the original data sets and the standard downsampled image within blue square from (b). The errors in (c) and (d) are shown by bright pixels. Note the significant reduction of errors with the MR sampled image.

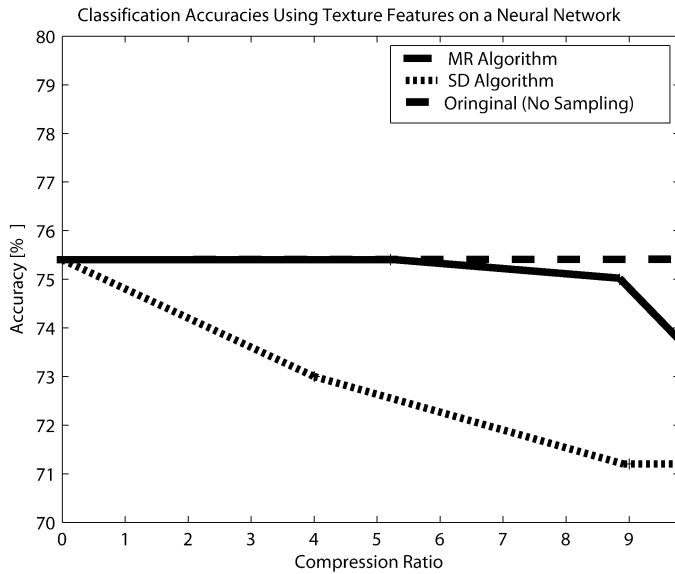


Fig. 13. Classification accuracy of the original system (no sampling), MR algorithm, and standard algorithm, using Haralick features and neural network classifier.

SVM was used to classify these features from approximated data sets. The training for this process are the features derived from the original data sets that have not undergone any down-sampling or approximation. Fig. 11 shows that the accuracy decline with standard downsampling is more drastic than that of the MR downsampling and the overall accuracy decline is minimal. Table I(a) gives the accuracy for each pattern class using the original data sets. Table I(b) shows the same detailed accuracy for MR downsampling with a compression ratio of 9:1, while Table I(c) shows the accuracy result with a compression ratio of 4:1. Note that the overall accuracy is identical for parts (b) and (c); however, the standard downsampling achieves this measure with more than twice the number of samples used by the MR approach.

TABLE II  
DETAILED CLASSIFICATION ACCURACY FOR (a) NO SAMPLING, (b) MR SAMPLING ALGORITHM, AND (c) SD ALGORITHM, USING HARALICK FEATURES AND NEURAL NETWORK CLASSIFIER

| Original Image Accuracy (No Sampling) |                      |    |     |     |    |     |     |     |     |     |
|---------------------------------------|----------------------|----|-----|-----|----|-----|-----|-----|-----|-----|
| Input                                 | Output of Classifier |    |     |     |    |     |     |     |     |     |
|                                       | DNA                  | ER | Gia | Gpp | L2 | Mit | Nuc | Act | TFR | Tub |
| DNA                                   | 92                   | 2  | 0   | 0   | 4  | 0   | 2   | 0   | 0   | 0   |
| ER                                    | 8                    | 72 | 0   | 0   | 0  | 8   | 0   | 0   | 0   | 12  |
| Gia                                   | 0                    | 0  | 84  | 10  | 2  | 4   | 0   | 0   | 0   | 0   |
| Gpp                                   | 0                    | 0  | 10  | 82  | 4  | 2   | 0   | 0   | 0   | 2   |
| L2                                    | 0                    | 0  | 0   | 6   | 76 | 2   | 0   | 0   | 12  | 4   |
| Nuc                                   | 2                    | 10 | 2   | 2   | 8  | 62  | 0   | 0   | 6   | 8   |
| Mit                                   | 0                    | 0  | 0   | 2   | 8  | 0   | 90  | 0   | 0   | 0   |
| Act                                   | 0                    | 0  | 2   | 0   | 0  | 2   | 2   | 88  | 0   | 6   |
| Tfr                                   | 0                    | 4  | 2   | 2   | 24 | 6   | 2   | 2   | 48  | 10  |
| Tub                                   | 2                    | 12 | 0   | 2   | 2  | 12  | 0   | 2   | 8   | 60  |

Average Accuracy: 75.4%

Accuracy with MR Algorithm

| Input | Output of Classifier |    |     |     |    |     |     |     |     |     |
|-------|----------------------|----|-----|-----|----|-----|-----|-----|-----|-----|
|       | DNA                  | ER | Gia | Gpp | L2 | Mit | Nuc | Act | TFR | Tub |
| DNA   | 90                   | 2  | 0   | 0   | 4  | 0   | 4   | 0   | 0   | 0   |
| ER    | 20                   | 68 | 0   | 0   | 2  | 4   | 0   | 0   | 0   | 6   |
| Gia   | 2                    | 0  | 82  | 8   | 2  | 4   | 0   | 2   | 0   | 0   |
| Gpp   | 0                    | 0  | 14  | 80  | 2  | 0   | 0   | 0   | 2   | 2   |
| L2    | 0                    | 0  | 4   | 2   | 80 | 0   | 8   | 0   | 4   | 2   |
| Nuc   | 2                    | 10 | 2   | 2   | 8  | 68  | 0   | 0   | 2   | 6   |
| Mit   | 0                    | 0  | 8   | 2   | 6  | 0   | 84  | 0   | 0   | 0   |
| Act   | 0                    | 0  | 2   | 0   | 0  | 2   | 2   | 88  | 0   | 6   |
| Tfr   | 0                    | 0  | 2   | 4   | 32 | 2   | 2   | 0   | 42  | 16  |
| Tub   | 2                    | 14 | 2   | 0   | 0  | 8   | 0   | 0   | 6   | 68  |

Average Accuracy: 75%, Compression Ratio: 8.9:1

Accuracy with SD Algorithm

| Input | Output of Classifier |    |     |     |    |     |     |     |     |     |
|-------|----------------------|----|-----|-----|----|-----|-----|-----|-----|-----|
|       | DNA                  | ER | Gia | Gpp | L2 | Mit | Nuc | Act | TFR | Tub |
| DNA   | 92                   | 4  | 0   | 0   | 4  | 0   | 0   | 0   | 0   | 0   |
| ER    | 24                   | 66 | 0   | 0   | 2  | 0   | 0   | 0   | 2   | 6   |
| Gia   | 0                    | 0  | 88  | 6   | 2  | 4   | 0   | 0   | 0   | 0   |
| Gpp   | 0                    | 0  | 16  | 78  | 0  | 0   | 4   | 0   | 2   | 0   |
| L2    | 0                    | 0  | 2   | 10  | 64 | 2   | 4   | 0   | 16  | 2   |
| Nuc   | 2                    | 14 | 2   | 2   | 8  | 56  | 0   | 0   | 10  | 6   |
| Mit   | 0                    | 0  | 4   | 4   | 16 | 0   | 76  | 0   | 0   | 0   |
| Act   | 0                    | 0  | 2   | 0   | 0  | 2   | 2   | 90  | 0   | 4   |
| Tfr   | 0                    | 4  | 0   | 6   | 28 | 4   | 2   | 0   | 42  | 14  |
| Tub   | 2                    | 16 | 0   | 0   | 0  | 14  | 0   | 0   | 8   | 60  |

Average Accuracy: 71.2%, Compression Ratio: 9:1

2) *Haralick Texture Features and Neural Network Classifier*: Now, we examine the results using Haralick texture features and the neural network classifier. We repeat the process of downsampling and feature calculation as above substituting the statistical features with texture features. We believe texture features to favor our algorithm based on the nature of the down-sampling schemes. Standard downsampling does not yield any additional resolution in areas where there are high frequencies, while MR sampling does preserve these frequencies (these high frequencies play a significant role in the determination of the texture features). Fig. 12 shows difference data sets for the two sampling schemes.

The preservation of high frequencies is further emphasized by the classification results. Fig. 13 shows that the level of sustained accuracy is much higher with our MR sampling algorithm and, in fact, is not affected by compression up to a ratio of 8. Table II shows the classification of the original data sets as well as downsampled data sets of using both sampling methods at similar compression ratios.

## VI. CONCLUSION

We presented a scheme for adaptive MR acquisition of fluorescence microscopy data sets in the context of classification of proteins based on their subcellular locations. We found that the MR downsampling outperforms standard downsampling due to an intelligent acquisition scheme. In a rate-distortion sense, our algorithm outperforms the standard one because it retains the high frequencies and saves samples where low frequencies are present. In terms of classification accuracy, our algorithm shows great promise as it significantly reduces the number of samples acquired while minimally affecting the classification accuracy. Future work includes implementing our algorithm as the microscope's scanning protocol.

## ACKNOWLEDGMENT

The authors would like to thank Prof. R. F. Murphy and E. Garcia Osuna. They would also like to thank Prof. T. Chen for valuable comments and T. Zhao for the use of his feature calculations and the classifier. The authors are indebted to Dr. Danuser for his comments.

## REFERENCES

- [1] J. Pawley, Ed., *Handbook of Biological Confocal Microscopy*. Madison, WI: IMR, 1995, pp. 1–17.
- [2] —, *Handbook of Biological Confocal Microscopy*. Madison, WI: IMR, 1995, pp. 139–154.
- [3] —, *Handbook of Biological Confocal Microscopy*. Madison, WI: IMR, 1995, pp. 267–279.
- [4] A. V. Oppenheim and R. W. Schaffer, "Sampling of continuous-time signals," in *Discrete-Time Signal Processing*, 2nd ed. Upper Saddle River, NJ: Prentice-Hall, 1999, ch. 4.
- [5] K. Huang and R. F. Murphy, "From quantitative microscopy to automated image understanding," *J. Biomed. Opt.*, vol. 9, pp. 893–912, 2004.
- [6] M. Velliste and R. F. Murphy, "Automated determination of protein subcellular locations from 3-D fluorescence microscope images," in *Proc. IEEE Int. Symp. Biomedical Imaging*, Washington, DC, 2002, pp. 867–870.
- [7] M. V. Boland and R. F. Murphy, "A neural network classifier capable of recognizing the patterns of all major subcellular structures in fluorescence microscope images of hela cells," *Bioinformatics*, pp. 1213–1223, 2001.
- [8] X. Chen and R. F. Murphy, "Robust classification of subcellular location patterns in high resolution 3-D fluorescence microscope images," in *Proc. Int. Conf. IEEE EMBS Soc.*, 2004, pp. 1632–1635.
- [9] J. Pawley, Ed., *Handbook of Biological Confocal Microscopy*. Madison, WI: IMR Press, 1995, pp. 327–346.
- [10] C. J. Cogswell and K. Carlsson, *Three-Dimensional Microscopy: Image Acquisition and Processing*. Bellingham, WA: SPIE, 1994.
- [11] J. C. Bulinski, D. J. Odde, Bo. J. Howell, T. D. Salmon, and C. M. Waterman-Storer, "Photobleaching and recovery of enscn5in chimera in untreated cells. Rapid dynamics of the microtubule binding of enscn5in in vivo," *J. Cell Sci.*, vol. 114, pp. 3885–3897, 2001.
- [12] K. Gonda, J. Fowler, N. Katoku-Kikyo, J. Haroldson, J. Wudel, and N. Kikyo, "Reversible disassembly of somatic nucleoli by the germ cell proteins FRGY2a and FRGY2b," *Nature Cell Biol.*, vol. 5, pp. 205–210, 2003.
- [13] E. A. J. Reits and J. J. Neeffjes, "From fixed to FRAP: Measuring protein mobility and activity in living cells," *Nature Cell Biol.*, pp. 145–147, 2001.
- [14] T. Zhao, private communication, 2004.
- [15] R. M. Haralick, "Statistical and structural approaches to texture," *Proc. IEEE*, vol. 67, no. 5, pp. 786–804, May, 1979.



**Thomas E. Merryman** (S'04) received the B.S. degrees in electrical engineering and computer engineering at North Carolina State University (NCSU), Raleigh, in December 2003. He is currently pursuing the Ph.D. degree at Carnegie Mellon University, Pittsburgh, PA.

At NCSU, he was an undergraduate in automatic target recognition with Dr. W. Snyder.



**Jelena Kovačević** (S'88–M'91–SM'96–F'02) received the Dipl. Electr. Eng. degree from the Electrical Engineering Department, University of Belgrade, Belgrade, Yugoslavia, in 1986 and the M.S. and Ph.D. degrees from Columbia University, New York, in 1988 and 1991, respectively.

From 1987 to 1991, she was a Graduate Research Assistant at Columbia University. In the summer of 1985, she was with Gaz de France, Paris, in the summer of 1987, she was with INTELSAT, Washington, DC, and in the summer of 1988, she was with Pacific Bell, San Ramon, CA. In the fall of 1986, she was a Teaching Assistant at the University of Belgrade. From 1991 to 2002, she was with Bell Labs, Murray Hill, NJ, as a Member of Technical Staff. She is a Co-Founder and Technical VP of xWaveforms, based in New York City. In 2003, she joined the Departments of Biomedical Engineering and Electrical and Computer Engineering, Carnegie Mellon University, Pittsburgh, PA, where she also serves as the Director of the Center for Bioimage Informatics. She was an Adjunct Professor at Columbia University. Her paper on multidimensional filter banks and wavelets, coauthored with M. Vetterli, was selected as one of the papers for inclusion in *Fundamental Papers in Wavelet Theory* (Princeton, NJ: Princeton University Press, 2004), edited by C. Heil and D. Walnut. She is a coauthor (with M. Vetterli) of the book *Wavelets and Subband Coding* (Englewood Cliffs, NJ: Prentice Hall, 1995). She is on the Editorial Boards of the *Journal of Applied and Computational Harmonic Analysis*, and the *Journal of Fourier Analysis and Applications*. Her research interests include wavelets, frames, biomedical signal processing, multirate signal processing, data compression, and signal processing for communications.

Dr. Kovačević received the Belgrade October Prize, the highest Belgrade prize for student scientific achievements awarded for the Engineering Diploma Thesis in October 1986, and the E. I. Jury Award at Columbia University for outstanding achievement as a graduate student in the areas of systems, communication, or signal processing. She is also a coauthor of the paper for which A. Mojsilovic received the Young Author Best Paper Award. She is the Editor-in-Chief of the IEEE TRANSACTIONS ON IMAGE PROCESSING. She served as an Associate Editor of the IEEE TRANSACTIONS ON SIGNAL PROCESSING and as a Guest Co-Editor (with I. Daubechies) of the Special Issue on Wavelets of the PROCEEDINGS OF THE IEEE. She was on the Editorial Board of the *IEEE Signal Processing Magazine*. She was Guest Co-Editor (with M. Vetterli) of the Special Issue on Transform Coding of the *IEEE Signal Processing Magazine* and Guest Co-Editor (with R. F. Murphy) of the Special Issue on Molecular and Cellular Bioimaging of the *IEEE Signal Processing Magazine*. She was a Member-at-Large of the IEEE Signal Processing Society Board of Governors and serves on the Bioimage and Signal Processing Technical Committee, as well as the Image and Multidimensional Signal Processing Technical Committee of the IEEE Signal Processing Society. She is the General Chair of the 2006 International Symposium on Biomedical Imaging, was the Co-Chair (with V. Goyal) of the DIMACS Workshop on Source Coding and Harmonic Analysis, and a General Co-Chair (with J. Allebach) of the 9th Workshop on Image and Multidimensional Signal Processing. She is a keynote speaker at ICAR05 and was a plenary speaker at DCC98 and SPIE98.